Synthesis and Characterization of a ZnO/CuO/Ag Composite and its Application as a Photocatalyst for Methyl Orange Degradation

Francisco A. Cataño[*], *Gustavo Cáceres, Ana Burgos, Ricardo S. Schrebler*

Instituto de Química, Facultad de Ciencias, Pontificia Universidad Católica de Valparaíso, Av. Universidad 330, Curauma, Valparaíso, Chile.
[*]E-mail: facatano@gmail.com

In this investigation we developed a supported photocatalytic system based on the Z-scheme. This system is of the type: zinc oxide nanorods (ZnO NRs)/cupric oxide nanoparticles (CuO NPs)/silver nanoparticles (Ag NPs). ZnO NRs were deposited electrochemically onto fluorine-doped tin oxide (FTO) thin films from $Zn(NO_3)_2$ aqueous solution. CuO NPs were obtained by a two-step synthesis involving the photodeposition of copper onto ZnO NRs, followed by heat treatment at 500°C for 1 hour. Ag NPs were deposited photochemically onto CuO NPs. Under illumination, the ZnO/CuO system follows Z-scheme charge separation and transfer mechanisms for the degradation of organic pollutants. The Ag nanoparticles on the CuO surface act as an electron scavenger from the conduction band, thus reducing the electron-hole recombination within the semiconductor. The photocatalytic activity was tested for the degradation of methyl orange.

Keywords: Heterogeneous photocatalysis, Z-scheme, zinc oxide, cupric oxide, photodeposition.

1. INTRODUCTION

Water is a vital resource for the sustenance of human life and biodiversity, and it is also a key element for the development of several economic activities in society. However, the accelerated growth of the human population and industrial activities has led to an increase in water pollution. Globally, over 80% of all wastewater is discharged without any treatment [1], leading to continued deterioration of rivers and the marine environment. Heterogeneous photocatalysis has been proven to be an alternative for the removal of hazardous and recalcitrant organic pollutants in water [2]. The possibility of using oxygen from the air as an oxidant and solar light as an energy source [3] makes heterogeneous photocatalysis an ideal technology for the treatment of wastewater. This technology is

based on the formation of highly reactive species on the surface of a semiconductor illuminated with photons of higher energy than the material bandgap. Unselective degradation of organic pollutants takes place in the aqueous phase through reaction with radical oxygen species (ROS) and photogenerated holes (h^+) [4]. Thus, in this context, the design and synthesis of efficient photocatalysts is of interest for the development and application of this technology.

Z-scheme photocatalytic systems have been used for water splitting, the removal of aqueous pollutants and CO_2 conversion [5]. This approximation is based on a two-step photoexcitation process using two different semiconductors with different bandgap energies (Figure 1). The idea behind this scheme is to obtain more available photogenerated electrons in the conduction band (CB) with higher reduction potential and more available photogenerated holes in the valence band (VB) with higher oxidation potential. This can be obtained by transferring photoexcited electrons in the semiconductor with the lower CB energy to the semiconductor with the higher VB energy [6]. In this manner, oxidation and reduction reactions occur with high overpotentials at different sites of the coupled semiconductor system [7].
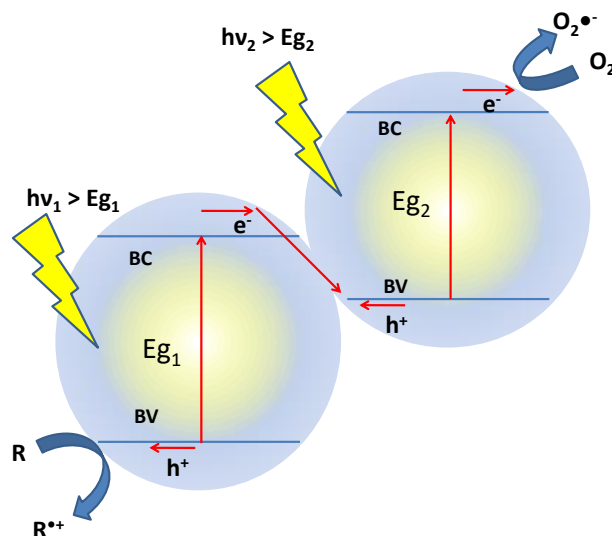
Figure 1. Z-scheme photocatalytic system for the degradation of organic pollutants.

To allow the easier transfer of photogenerated electrons from one semiconductor to another, a conductive material between the two semiconductors is used as an electron mediator [8]. The design of an efficient Z-scheme photocatalytic system without a conductive mediator could simplify the fabrication procedures and reduce the cost of the system. One alternative for maintaining efficient photoelectron transfer without any conductive material consists of using two semiconductors, in which the positions of the lower CB and the higher VB are similar [9]. It has been found a photoexcited electron injection from CdS into ZnO [10], besides the coupled ZnO/CdS heterostructure, has shown photocatalytic activity in water splitting by the Z-scheme [6,11]. The use of CuO instead of CdS could improve the photoelectron transfer due to more appropriate band positions; the valence bands of CdS and CuO are located at -6.20 eV [12-13] and -5.42 eV [14] with respect to the vacuum level, respectively, whereas the conduction band of ZnO is located at -4.40 eV [15].

The coupling of ZnO and CuO has been used for the photocatalytic production of hydrogen [16], photocatalytic degradation of aqueous pollutants [17,18], solar cells [19] and CO_2 photoreduction [20]. These materials are low cost, abundant and nontoxic; therefore, they are ideal for environmental applications. This system satisfies the requirements for the energy band positions of the Z-scheme [20-22], with CuO being the semiconductor with the higher CB energy. In addition, ZnO is an n-type semiconductor [23] and CuO is a p-type semiconductor [24]. Thus, under illumination, the holes in the VB of the ZnO and the electrons in the CB of the CuO will diffuse spontaneously into the semiconductor/aqueous solution interface [25], therefore favoring the charge transfer reactions involved in the Z-scheme.

One of the ways of improving the photocatalytic activity of semiconductors is by the deposition of noble metal nanoparticles, such as Pt, Au and Ag [26-27]. These metals can act as an electron scavenger, reducing the electron-hole recombination rate within the semiconductor and thus improving the kinetics of photocatalytic reactions [28]. The electrons can be further transferred to molecular oxygen to produce superoxide anion radicals and subsequently other ROS [29]. Due to its low cost and easy deposition, Ag is a good alternative that can be used to boost the photocatalytic activity of a semiconductor.

In this work, a supported photocatalytic system was developed via electrochemical and photochemical methods. This system consists of ZnO NRs grown onto FTO substrates, in which CuO NPs, and then Ag NPs are deposited photochemically. To obtain a selective deposition of Ag onto CuO, the photodeposition of Ag was performed while cutting off ultraviolet radiation. The use of a photocatalyst supported on a substrate avoids the processes associated with the separation and recovery of the photocatalyst; on other hand, structures such as nanowires and nanorods show a high surface area and better light absorption by scattering [30]. Structural, morphological and optical characterization of the film was performed, and the photocatalytic activity was evaluated for the degradation of methyl orange. The observed increases in photocatalytic activity with the incorporation of CuO NPs and Ag NPs are analyzed in terms of the generation, separation, recombination and reactions of charge carriers.

2. EXPERIMENTAL

2.1. ZnO Electrodeposition

The electrodeposition of ZnO films onto FTO substrates was carried out similarly to a previous report [31]. Briefly, the deposits were obtained at constant potential of -0.8 V vs Ag/AgCl$_{(sat)}$ over 3 hours. The electrolytic bath consisted of a 0.01 M Zn(NO$_3$)$_2$ aqueous solution at 80°C. A platinum wire was used as the counter electrode, and the electrodeposition potential was controlled by a Gamry Serie G750 potentiostat. Previous to their use, FTO substrates were successively rinsed with distilled/deionized water and dimethyl ketone in an ultrasonic bath. To eliminate dissolved oxygen, argon was bubbled through prior to the deposition process. The exposed area of the working electrode was 2.0 x 2.0 cm^2. The final samples were washed with distilled/deionized water to remove any residual salt and dried with an argon flow.

2.2. CuO deposition

The ZnO films were immersed in a quartz cell containing 15 mL of an aqueous solution of 0.16 mM $CuSO_4$ and 1% v/v CH_3OH. Then, the substrates were illuminated employing a 1000 W Xe/Hg lamp (Oriel 6295) at room temperature for 2 hours. The sample's distance to the light source was maintained at 5.0 cm. To avoid the overheating of the aqueous solution, the infrared radiation was eliminated through a water filter. Under these conditions, the range of wavelengths used was between ~240 nm and ~950 nm. This filter and lamp were also used in the other experiments of this work. Since the dissolved oxygen can act as an electron acceptor, argon was bubbled through prior to and during the photodeposition process. Finally, the samples were washed with distilled-deionized water, dried with an argon flow and calcined at 500°C for 1 h.

2.3. Ag deposition

The photodeposition of Ag was performed in a similar way as that described for the CuO photodeposition. In this case, the ZnO/CuO films were immersed in a quartz cell containing 15 mL of aqueous solution of 0.6 mM $AgNO_3$ and 1% v/v CH_3OH. Additionally, a filter was used to cut off the ultraviolet radiation ($\lambda < 399$ nm). The illumination time was 40 min. Argon bubbling was also maintained prior to and during the photodeposition process. The samples were washed with distilled-deionized water and methanol. Finally, they were dried with an argon flow. No heat treatment was applied on the final ZnO/CuO/Ag film.

2.4. Photocatalytic activity test

The photocatalytic activities of the different films were estimated by measuring the degradation of methyl orange (MO). A quartz cell containing 15 mL of a 20 ppm dye solution was placed in front of the light source. Then, the photocatalytic films were immersed in the solution, and the distance between the films and the lamp was kept at 5.0 cm. Before the photodegradations, the supported photocatalysts were held for one hour in the dark with permanent air bubbling through the solution with the aim of reaching the adsorption-desorption equilibrium and ensuring dissolved oxygen saturation. Then, the lamp was switched on to initiate the reaction, with this time being t = 0. The photodegradations were carried out for 160 min, and samples were taken every 40 min. The dye concentration was measured with the absorption at $\lambda_{max} = 464.8$ nm, and the respective values were extracted from a previously recorded calibration curve.

2.5. Structural, morphological and optical characterization

The crystal structures of the supported photocatalyst were characterized with a Bruker D8 Advance A25 model X-ray diffractometer (40 kV, 40 mA, Cu-Kα radiation with $\lambda = 1.5406$ Å). The morphology of the films was investigated using a scanning electron microscope (SEM Hitachi

SU3500) equipped with an energy-dispersive X-ray analysis (EDX) attachment. Optical properties were studied by transmission and absorption spectroscopy using a Shimadzu UV-1800 UV spectrophotometer.

3. RESULTS AND DISCUSSION

3.1. Structural Characterization

The electrochemical synthesis of ZnO films employing $Zn(NO_3)_2$ aqueous solutions is based upon the formation of hydroxide ions from the reduction of nitrate with the consequent precipitation of $Zn(OH)_2$ onto the FTO substrate (eq. 1 and 2). [32]. At high temperatures, $Zn(OH)_2$ is dehydrated to form ZnO (eq. 3) [33].

$$NO_3^- + H_2O + 2e^- \rightarrow NO_2^- + 2OH^- \qquad (1)$$
$$Zn^{2+} + 2OH^- \rightarrow Zn(OH)_2 \qquad (2)$$
$$Zn(OH)_2 \rightarrow ZnO + H_2O \qquad (3)$$
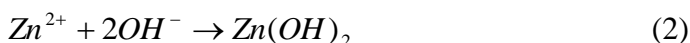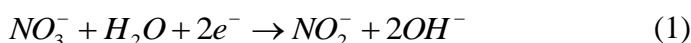
In this work, electrodeposited ZnO is used as a substrate for CuO deposited by a two-step process. In the first step, the photoexcitation of ZnO leads to the formation of an electron-hole pair. Copper(II) ions are reduced by photogenerated electrons in the conduction band of ZnO to form metallic copper. On the other hand, the holes in the valence band can oxidize both water and methanol. Then, CuO is formed by calcination.
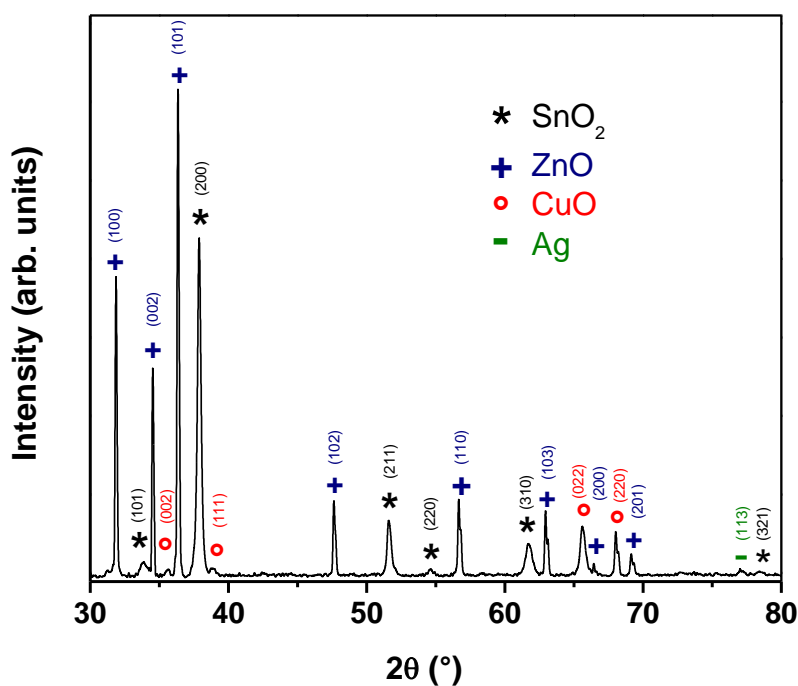
Figure 2. X-ray diffraction pattern of the ZnO/CuO/Ag supported heterostructure.

The same principle applies to the photodeposition of Ag; in this case, due to only light in the visible range of the spectrum was used, the electron-hole pairs were generated within the CuO NPs. To probe the formation of ZnO, CuO, and Ag, X-ray diffraction (XRD) experiments were carried out. Figure 2 shows the XRD patterns of the supported heterostructure. All of the observed diffraction peaks can be indexed to four different crystal phases: hexagonal ZnO (JCPDS, 5-0664), monoclinic CuO (JCPDS, 48-1548), cubic Ag (JCPDS, 04-0783) and tetragonal SnO_2 (JCPDS, 41-1445). The peaks from tetragonal SnO_2 are related to the FTO/glass used as the substrate. Eight diffraction peaks corresponding to the (100), (002), (101), (102), (110), (103), (200) and (201) planes of the ZnO hexagonal wurtzite structure can be clearly identified. In addition, four diffraction peaks related to the (002), (111), (022) and (220) planes of monoclinic CuO are identified. All of the peaks of ZnO as well as the peaks (022) and (220) of CuO are intense and well defined, indicating a high crystallinity of the phases.

To corroborate the photodeposition of Ag, other XRD measurements were obtained using a parallel beam in the grazing incidence configuration. In this configuration, the angle of the incident beam remains constant (θ_i) while the detector angle moves 2θ. In this manner, a lower penetration of the X-ray beam through the surface can be obtained, avoiding the contribution of the substrate. Figure 3 shows the obtained grazing-incidence XRD pattern.
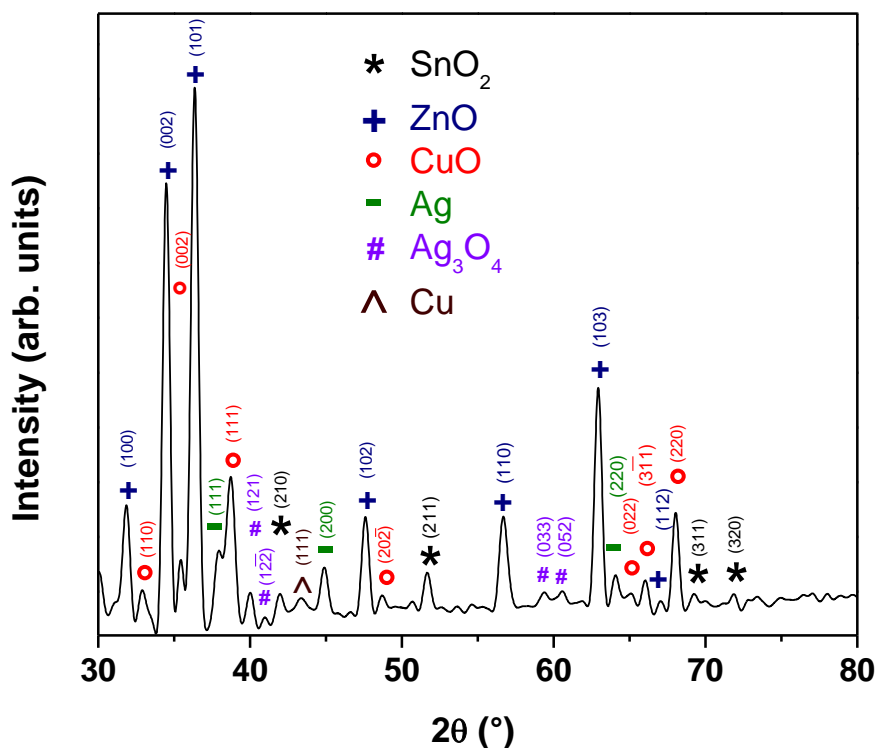
Figure 3. Grazing-incidence X-ray diffraction patterns of the ZnO/CuO/Ag supported heterostructure.

Diffraction peaks corresponding to hexagonal ZnO and monoclinic CuO are clearly identified. As expected, the relative intensities of the SnO_2 peaks with respect to the ZnO and CuO peaks diminish significantly. Three peaks corresponding to the (111), (200) and (220) planes of cubic Ag are

also present. These peaks are well defined, indicating the successful photodeposition of Ag. However, some small extra diffraction peaks were observed, and these peaks can be related to monoclinic Ag_3O_4 (JCPDS, 84-1261) and cubic Cu (JCPDS, 04-0836). The low intensities of these peaks indicate that these spurious phases are present in a very small amount with respect to the other deposited phases.

3.2. Morphological Characterization

Figure 4a and b show the SEM images of the ZnO electrodeposited onto FTO substrates. The deposited films consist of a dense array of NRs of hexagonal shape, in which the diameter of the hexagonal cross section decreases from the bottom to the top of the structure. This feature was also observed in a previous report [31]. Additionally, the ZnO NRs grow inclined with respect to the substrate and have a diameter between 700 and 300 nm.
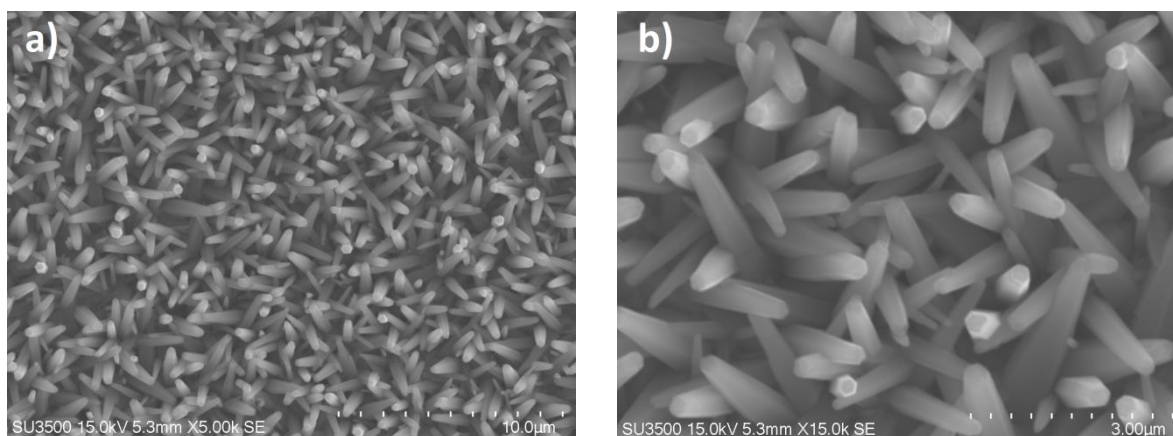
Figure 4. SEM images of the ZnO NRs array.

The photodeposition of CuO and Ag leads to the formation of nanoparticles over the surface of ZnO (Figure 5a and b). These nanoparticles are well dispersed over the NRs and only partially cover them. There are no significant differences between the SEM images of the samples with and without the photodeposition of Ag, and thus, we can conclude that Ag is present in a smaller quantity than CuO. The elemental composition of the heterostructure was obtained by EDX analysis. Assuming a 1:1 stoichiometry for the metal and oxygen in ZnO and CuO, we obtained the following phases composition in terms of the mass percentage: ZnO: 86.28%, CuO: 13.55% and Ag: 0.17%. Clearly, ZnO is the main constituent in the heterostructure followed by CuO. The Ag content is approximately 1.2 wt% of CuO. In addition, due to the synthetic procedure, Ag is present preferentially over CuO NPs.
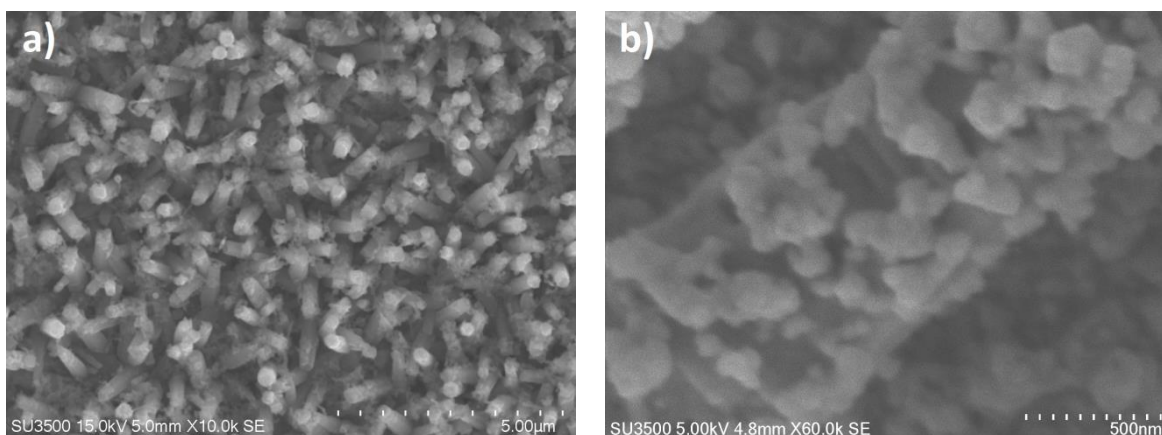
Figure 5. SEM images of the ZnO/CuO/Ag heterostructures.

3.3. Optical Characterization

To study the optical properties of the supported heterostructure, a UV-vis transmittance spectrum was taken (Figure 6a). This spectrum is characterized by a continuous transmittance increase from the near-UV region to 900 nm, followed by a decrease. The absorbance spectrum (Figure 6b) can be obtained employing the equation: $\alpha_{exp} \approx -Ln(T)$ [34], where α_{exp} is the experimental absorption coefficient. The absorption coefficient presents two increases at approximately 1.4 eV and 3.2 eV, and these increases are associated with electronic transitions from the valence bands to the conduction bands of CuO and ZnO, respectively.
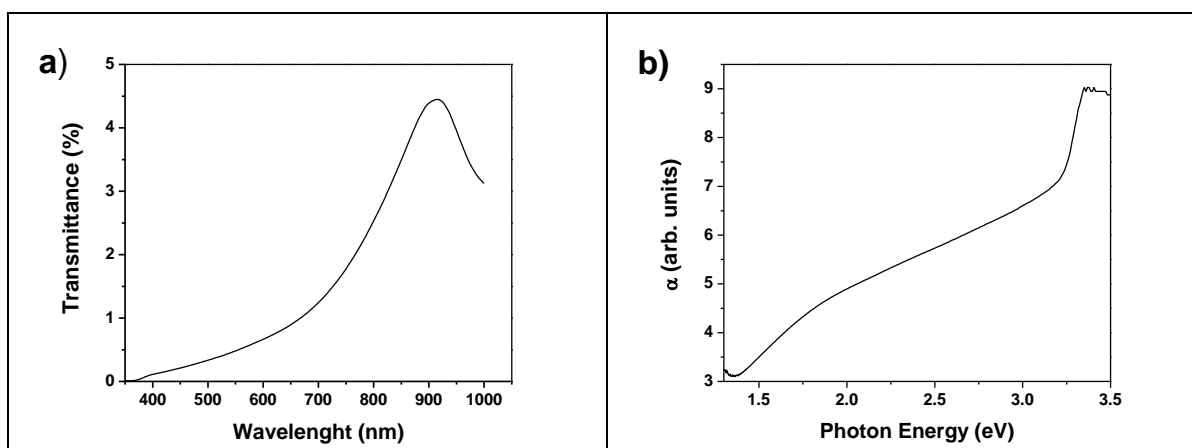
Figure 6. a) Transmittance spectrum and b) absorbance spectrum of the supported heterostructure.

The first estimate of the optical bandgap of the semiconductors was obtained from the peak positions in the graph of $dT/d\lambda$ (first derivative of T against wavelength λ) [35] (Figure 7). Indeed, $dT/d\lambda$ has two prominent peaks centered at 385 nm and 861 nm. From these wavelengths, we obtain bandgap energies of 1.44 eV and 3.22 eV for CuO and ZnO, respectively.
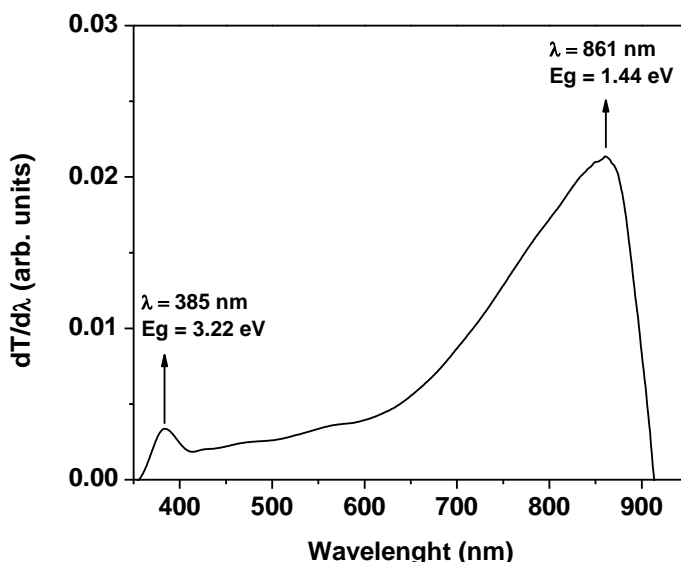
Figure 7. First derivative of the transmittance *T* against λ. Each peak corresponds to an estimation of the optical bandgap of the semiconductors in the heterostructure.

The reported bandgap energies for CuO are between 1.2 eV and 1.7 eV with a direct optical transition [36,37]. However, a joint experimental and theoretical study has predicted and measured an indirect bandgap of 1.24 eV apart from a direct bandgap of 1.46 eV [38]. Depending on the band structure of the semiconductor, both transitions, direct and indirect, can occur.
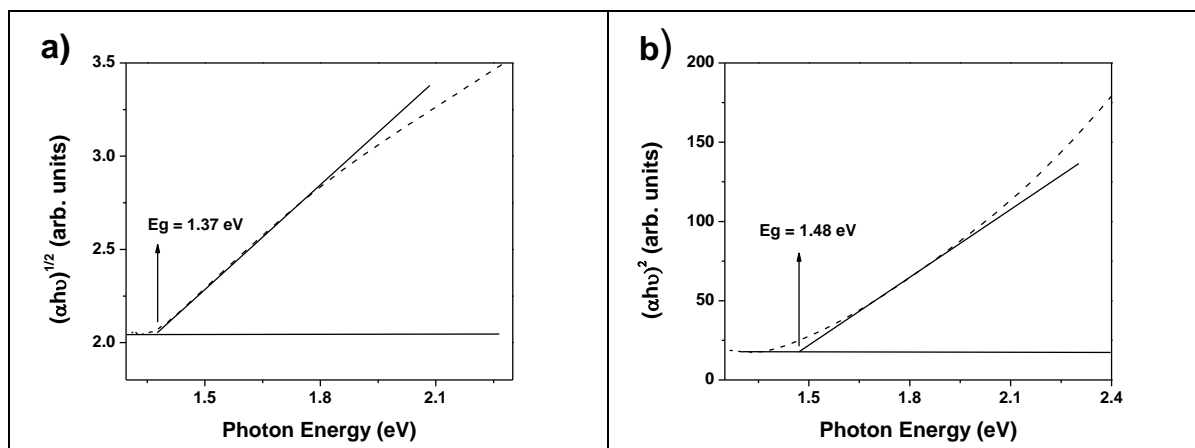
Figure 8. Optical bandgap energies estimated for CuO: a) indirect transition and b) direct transition.

The bandgap energy can be obtained by a linear fitting of the $(\alpha h v)^n$ vs hv plot; the intercept of this linear fit with the zero line absorption ($\alpha = 0$) is the bandgap energy. For a direct transition, n = 2, and for an indirect transition, n = ½. Figure 8a and b show the $(\alpha h v)^n$ vs hv plots and the obtained bandgap energies for indirect and direct transitions, respectively. For each estimation of the bandgap energy, the baseline or zero absorption line must be taken into account. This baseline corresponds to the region of the plot at lower energy than the bandgap [39] and represents the effects of the reflections, dispersions and sub-bandgap absorption [34]. The bandgap energies obtained are 1.37 eV

for indirect transitions and 1.48 eV for direct transitions. These values are close to those obtained by the $dT/d\lambda$ method and are in agreement with the reported values cited above. Another interesting aspect is the fact that the value of the direct bandgap energy is closer to the peak position in the plot of $dT/d\lambda$ than the indirect bandgap, suggesting that the optical behavior of the CuO is mostly defined by direct transitions. Indeed, the absorption coefficients associated with direct transitions are much higher than for indirect transitions [40].
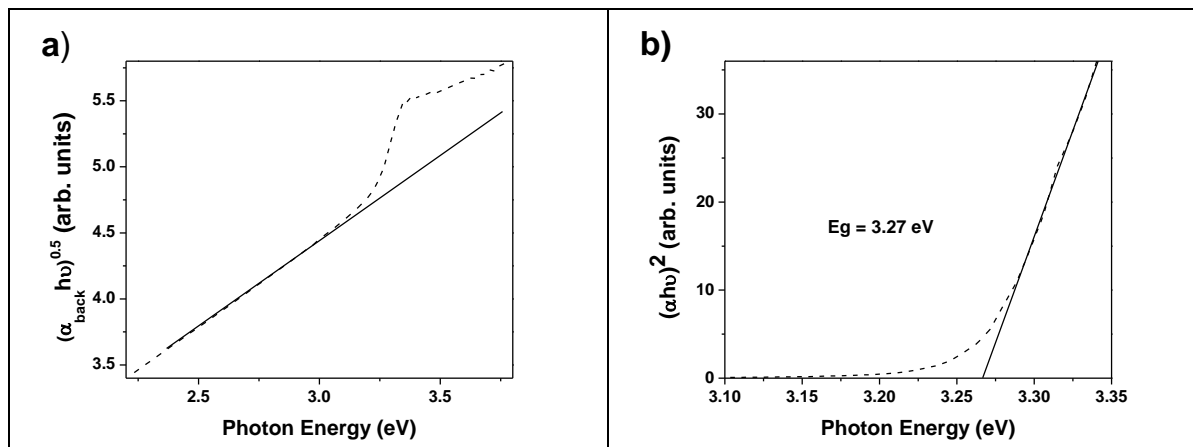
Figure 9. Procedure for deriving the bandgap energy of ZnO: a) α_{back} estimation and b) energy bandgap determination.

ZnO is a semiconductor with a direct optical transition and reported bandgap energies between 3.2 and 3.4 eV [41]. The determination of the optical bandgap of ZnO was performed by modeling the zero line absorption as an indirect absorption coefficient, α_{back}. Then, the direct absorption coefficient is obtained by subtracting α_{back} from α_{exp} ($\alpha_{dir} = \alpha_{exp} - \alpha_{back}$). This methodology has been applied previously in the optical analysis of supported ZnO nanowires [35]. Figure 9a shows the linear fitting for the determination of α_{back}, while Figure 9b shows the $(\alpha h\nu)^2$ vs $h\nu$ plot. The obtained bandgap energy value was 3.27 eV; as in the case of CuO, this value is similar to that obtained by the $dT/d\lambda$ method.

3.4. Photocatalytic activity

The photocatalytic activities of the different samples were evaluated following the degradation of MO under UV-vis illumination. Figure 10a, b and c show the evolution of the spectral absorption of an MO solution during heterogeneous photocatalysis using the ZnO, ZnO/CuO and ZnO/CuO/Ag films, respectively. In all cases, the absorbance decreases with irradiation time, indicating that MO is chemically transformed. However, the illumination of a bare FTO/glass substrate immersed in the aerated dye solution did not produce significant changes in the spectral absorption, indicating that the observed degradations are due to the photocatalytic activities of the different samples.
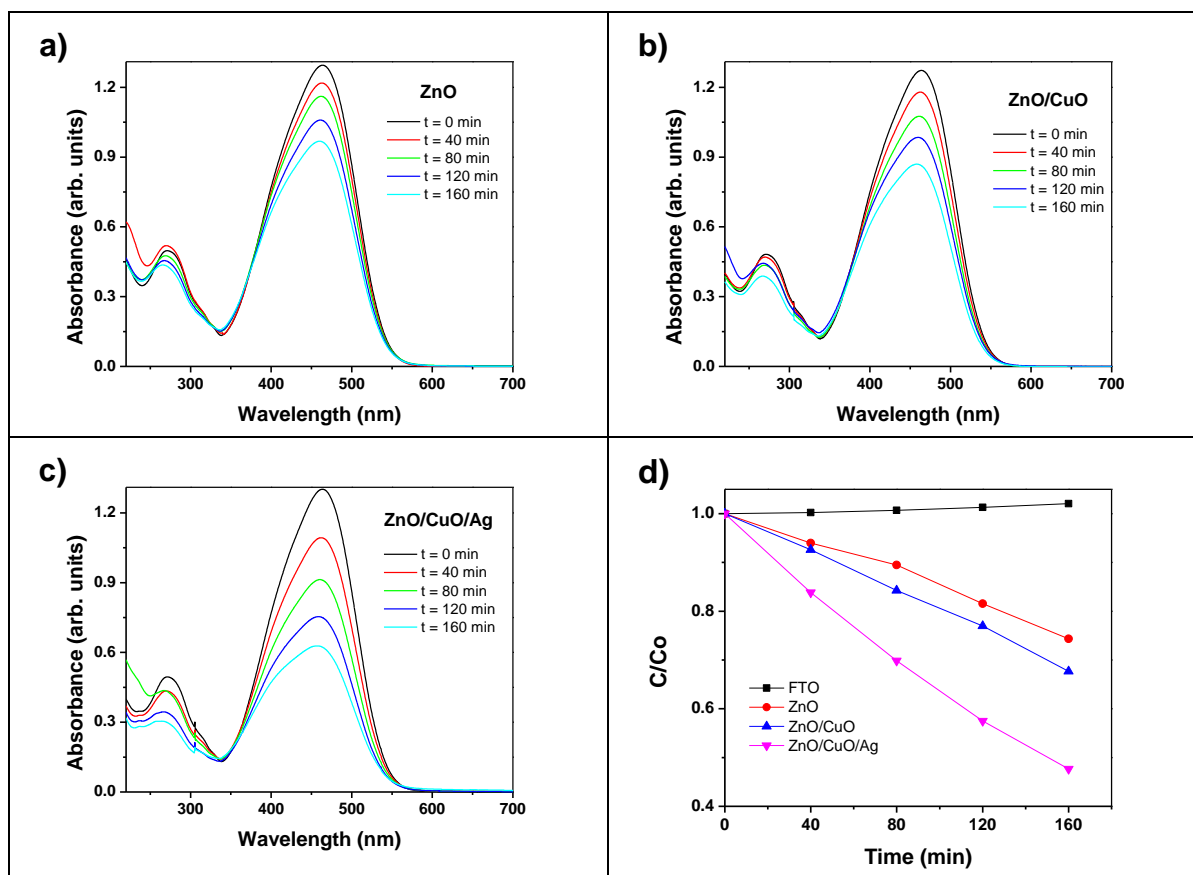
Figure 10. Absorption spectra evolution of MO (20 ppm) solution during heterogeneous photocatalysis using: a) ZnO, b) ZnO/CuO and c) ZnO/CuO/Ag; d) Changes in the MO concentration over the course of the photocatalytic degradation.

Figure 10d shows the decrease in the dye concentration estimated from its absorbance at $\lambda_{max} = 464.8$ nm. It can be observed that the photocatalytic activity increases first with the incorporation of CuO NPs and then with Ag NPs. The higher photocatalytic activity of the ZnO NRs/CuO NPs heterostructure relative to bare ZnO NRs could be explained taking into account optical and mechanistic aspects. First, CuO is a semiconductor with a narrow bandgap that can be activated with visible light, while ZnO has a wide bandgap and is active under ultraviolet light. The use of two semiconductors with different bandgap energies leads to a stronger light absorption with a wide spectral response. As a consequence, a higher rate of electron-hole pair generation is achieved.

From the mechanistic point of view, as is established in the Z-scheme, the coupling of ZnO and CuO take advantage of the higher reduction potential of the BC of CuO for interfacial reduction reactions and the higher oxidation potential of the VB of ZnO for interfacial oxidation reactions. Additionally, the p-type conductivity of CuO and the n-type conductivity of the ZnO lead to a charge-carrier flow that favors reduction reactions over CuO NPs and oxidation reactions over ZnO NRs. In this manner, oxidation and reduction reactions are carried out at high rates on different sites of the heterostructure.

Under UV-vis illumination, both ZnO and CuO are excited. The photogenerated electrons in the CB of ZnO could be transferred to the VB of CuO because the CB of ZnO is more negative than

the VB of CuO. Hence, the photogenerated holes tend to remain in the VB of ZnO, whereas the photogenerated electrons tend to remain in the CB of CuO. The high oxidation potential of the photogenerated holes in the VB of ZnO permits the direct oxidation of MO to reactive intermediates. Hydroxyl radicals are also generated due that the VB position of ZnO (2.98 V) is more positive than the potential of the couples OH$^•$/OH$^-$ and OH$^•$/H$_2$O [11]. These radicals are highly reactive species and can lead to MO degradation. The Ag NPs enhance the kinetic of the photocatalytic process acting as an electron trap, inhibiting the electron-hole recombination within CuO NPs. Furthermore, the trapped electrons and electrons in the CB of CuO reduce molecular oxygen to form superoxide anion radicals, which can accelerate the organic dye degradation [42]. The proposed mechanism of the photocatalytic degradation is schematized in Figure 11.
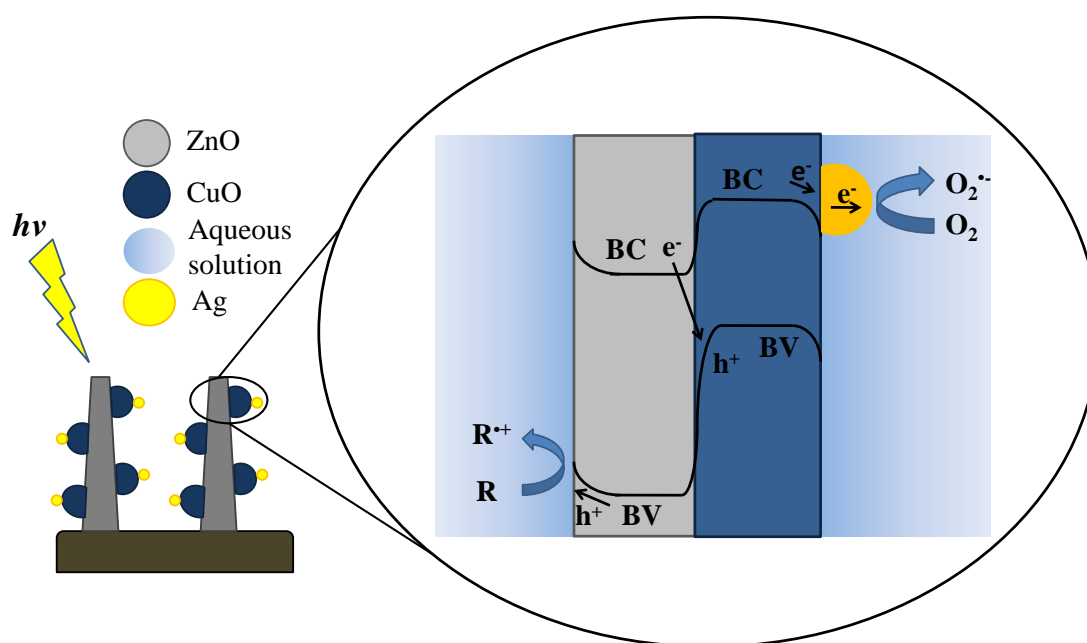
Figure 11. Proposed mechanism for the photocatalytic degradation of MO.

For comparison, Table 1 shows some reported results of the photodegradation of MO using different supported photocatalysts. Due to that the efficiency of the photocatalytic processes strongly depends on the experimental conditions such as the initial concentration of the organic compound, air bubbling, hydrodynamics, temperature, photon flux, mass of immobilized photocatalyst, pH, etc., the results of Table 1 cannot be taken as an accurate comparison of the activities of the photocatalysts toward the degradation of MO. Additionally, it is reasonable to assume that for a given photocatalyst and an initial concentration of MO, the percentage of degradation is proportional to the geometric area of the photocatalyst and the illumination time, and thus, for comparison, we normalized the amount of dye degradation per unit of geometric area and time (eq. 4):

$$\frac{V(C_0 - C)}{St} \qquad (4)$$

where V is the volume, C_0 is the initial concentration of MO, C is the final concentration of MO, S is the geometric area of the photocatalyst and t is the time. Great differences between the photocatalytic activities can be observed. Our results are satisfactory; however, further work will be devoted to optimizing the photocatalytic activity of the proposed photocatalyst.

Table 1. Comparison of some results of the photodegradation of MO using different supported photocatalysts.

Ref	Photocatalyst	Lamp	C_0 (mg/L)	V (mL)	Geometric area (cm^2)	% degradation	Time (min)	$\dfrac{V(C_0-C)}{St}$ (mg/cm^2.min)
43	ZnO	300 W High pressure Hg	20	20	4	100	50	0.002
44	TiO$_2$/Ag	Black light	6.2	5	0.8	90	60	0.00058
45	TiO$_2$/W$_{10}$O$_{32}$	300 W Medium pressure Hg	20 pH=2	20	29.0322	84.09	90	0.00013
46	ZnO	254 nm UV Light	6.5	500	432.75	93.05	160	0.00004
This study	ZnO/CuO/Ag	Xe/Hg 1000 W	20	15	4	52.34	160	0.00024

4. CONCLUSIONS

A supported photocatalytic system based on ZnO NRs/CuO NPs/Ag NPs was developed via electrochemical and photochemical methods. X-ray diffraction patterns demonstrate the formation of ZnO, CuO and Ag. The transmittance spectrum of the heterostructure was used to obtain the optical bandgaps of the semiconductors; a direct bandgap of 3.22 eV was estimated for ZnO, while those for CuO were estimated as 1.37 eV and 1.48 eV for indirect and direct transitions, respectively. The photocatalytic activity was evaluated for the degradation of MO, and the results show an increase in the photocatalytic activity with the incorporation of CuO NPs and Ag NPs. The effect of CuO on the photocatalytic activity was attributed to an enhancement in the optical response and to a Z-scheme-type mechanism. Ag NPs improve the photocatalytic activity by reducing the electron-hole recombination by accepting electrons from the conduction band and therefore favoring the charge transfer reactions involved in the Z-scheme.

References

1. United Nations World Water Assessment Programme, The United Nations World Water Development Report 2017. Wastewater: The Untapped Resource, UNESCO, (2017) Paris, France.
2. D. Li, Q. Zhu, C. Han, Y. Yang, W. Jiang, Z. Zhang, *J. Hazard. Mater.,* 285 (2015) 398.
3. D. Robert, S. Malato, *Sci. Total Environ.*, 291 (2002) 85.
4. V. Augugliaro, M. Bellardita, V. Loddo, G. Palmisano, L. Palmisano, S. Yurdakal, *J. Photochem. Photobiol. C*, 13 (2012) 224.
5. P. Zhou, J. Yu, M. Jaroniec, *Adv. Mater.*, 26 (2014) 4920.
6. X. Wang, G. Liu, Z-G. Chen, F. Li, L. Wang, G.Q. Lu, H-M. Cheng, *Chem. Commun.*, 23 (2009) 3452.
7. J. Fu, S. Cao, J. Yu, *J. Materiomics*, 1 (2015) 124.
8. K. Qi, B. Cheng, J. Yu, W. Ho, *Chin. J. Catal.*, 38 (2017) 1936.
9. F.Q. Zhou, J.C. Fan, Q.J. Xu, Y.L, Min, *Appl. Catal., B*, 201 (2017) 77.
10. L. Spanhel, H. Weller, A. Henglein, *J. Am. Chem. Soc.*, 109 (1987) 6632.
11. D. Ma, J-W. Shi, Y. Zou, Z. Fan, X. Ji, C. Niu, L. Wang, *Nano. Energy*, 39 (2017) 183.
12. Q. Lu, Y. Yu, Q. Ma, B. Chen, H. Zhang, *Adv. Mater.*, 28 (2016) 1917.
13. X. Lou, G. Wang, Y. Huang, B. Wang, H. Yuan, H. Chen, *Phys. Chem. Chem. Phys.*, 19 (2017) 28216.
14. F.P. Koffyberg, F.A. Benko, *J. Appl. Phys.*, 53 (1982) 1173.
15. T-W. Zeng, I-S. Liu, F-C. Hsu, K-T. Huang, H-C. Liao, W-F. Su, *Opt. Express.*, 18 (2010) 130137.
16. Z. Liu, H. Bai, S. Xu, D.D. Sun, *Int. J. Hydrogen. Energy,* 36 (2011) 13473.
17. R. Saravanan, S. Karthikeyan, V.K. Gupta, G. Sekaran, V. Narayanan, A. Stephen. *Mater. Sci. Eng. C,* 33 (2013) 91.
18. S. Chabri, A. Dhara, B. Show, D. Adak, A. Sinha, N. Mukherjee, *Catal. Sci. Technol.*, 6 (2016) 3238.
19. S. Hussain, C. Cao, G. Nabi, W.S. Khan, M. Tahir, M. Tanveer, I. Aslam, *Optik.*, 130 (2017) 372.
20. W-N. Wang, F. Wu, Y. Myung, D.M. Niedzwiedzki, H.S. Im, J. Park, P. Banerjee, P. Biswas, *ACS. Appl. Mater. Interfaces*, 7 (2015) 5685.
21. X. Zhao, P. Wang, B. Li, *Chem. Commun.*, 46 (2010) 6768.
22. M. Hussain, Z.H. Ibupoto, M.A. Abbassi, A. Khan, G. Pozina, O. Nur, M. Willander, *J. Nanoelectron. Optoe.*, 9 (2014) 1.
23. M.D. McCluskey, S.J. Jokela, *Physica B,* 401-402 (2007) 355.
24. Y.K. Jeong, G.M. Choi, *J. Phys. Chem. Solids*, 57 (1996) 81.
25. M. Gratzel, *Nature*, 414 (2001) 338.
26. M. Ni, M.K.H. Leung, D.Y.C. Leung, L.K. Sumathy, *Renew. Sust. Energ. Rev.*, 11 (2007) 401.
27. P.V. Kamat. *J. Phys. Chem. Lett.*, 3 (2012) 663.
28. A.V. Rupa, D. Manikandan, D. Divakar, T. Sivakumar, *J. Hazard. Mater.*, 147 (2007) 906.
29. H.M. Sung-Suh, J.R. Choi, H.J. Hah, S.M. Koo, Y.C. Bae, *J. Photochem. Photobiol., A*, 163 (2004) 37.
30. Y. Liu, J, Han, W. Qiu, W. Gao, *Appl. Surf. Sci.*, 263 (2012) 389.
31. F.A. Cataño, H. Gómez, E.A. Dalchiele, R.E. Marotti, *Int. J. Electrochem. Sci.*, 9 (2014) 534.
32. T. Yoshida, D. Komatsu, N. Shimokawa, H Minoura, *Thin Solid Films*, 451-452 (2004) 166.

33. M. Guo, C.Y. Yang, M. Zhang, Y.J. Zhang, T. Ma, X.D. Wang, X.D. Wang, *Electrochim. Acta*, 30 (2008) 4633.
34. G. Guerguerian, F. Elhordoy, C.J. Pereyra, R.E. Marotti, F. Martín, D. Leinen, J.R. Ramos-Barrado, E.A. Dalchiele, *J. Phys. D: Appl. Phys.*, 45 (2012) 245301.
35. C.D. Bojorge, V.R. Kent, E. Teliz, H.R. Cánepa, R. Henríquez, H. Gómez, R.E. Marotti, E.A. Dalchiele, *Phys. Status Solidi A*, 208 (2011) 1662.
36. D. Chauhan, V.R. Satsangi, S. Dass, R. Shrivastav, *Bull. Mater. Sci.*, 29 (2006) 709.
37. M.R. Johan, M.S.M. Suan, N.L. Hawari, H.A. Ching, *Int. J. Electrochem. Sci.*, 6 (2011) 6094.
38. Y. Wang, S. Lany, J. Ghanbaja, Y. Fagot-Revurat, Y.P. Chen, F. Soldera, D. Horwat, F. Mücklich, J. F. Pierson, *Phys. Rev. B*, 94 (2016) 245418.
39. A. Burgos, F. Cataño, B. Marí, R. Schrebler, H. Gómez, *J. Electrochem. Soc.*, 163 (2016) D562.
40. R. Memming, Semiconductor Electrochemistry, WILEY-VCH, (2000) Weinheim, Germany.
41. R.E. Marotti, P. Giorgi, G. Machado, E.A. Dalchiele, *Sol. Energy Mater. Sol. Cells*, 90 (2006) 2356.
42. Y. Li, J. Niu, L. Yin, W. Wang, Y. Bao, J. Chen, Y. Duan, *J. Environ. Sci.*, 23 (2011) 1911.
43. F. Xu, Y. Shen, L. Sun, H. Zeng, Y. Lu, *Nanoscale,* 3 (2011) 5020.
44. I.M. Arabatzis, T. Stergiopoulus, M.C. Bernard, D. Labou, S.G. Neophytides, P. Falaras, *Appl. Catal., B*, 42 (2003) 187.
45. P. Niu, J. Hao, *Colloids Surf. A*, 431 (2013) 127.
46. Y.L. Chen, L.C. Kuo, M.L. Tseng, H.M. Chen, C.K. Chen, H.J. Huang, R.S. Liu, D.P. Tsai, *Opt. Express,* 21 (2013) 7240.